Colloids and Surfaces A: Physicochemical and Engineering Aspects 627 (2021) 127075

Contents lists available at ScienceDirect

Colloids and Surfaces A: Physicochemical and Engineering Aspects

journal homepage: www.elsevier.com/locate/colsurfa

Superhydrophobic and nanostructured CuFeCo powder alloy for the capture of microplastics

Oriol Rius-Ayra *, Alisiya Biserova-Tahchieva *, Isabel López-Jiménez, Nuria Llorca-Isern

CMQF Departament de Ciència dels Materials i Química Física, Universitat de Barcelona, Martí i Franquès 1–10, 08028, Barcelona, Spain

HIGHLIGHTS

- Nanostructured CuFeCo particles acquire superhydrophobicity through functionalisation with dodecanoic acid.
- The superhydrophobic CuFeCo particles separate oil from water.
- The superhydrophobic CuFeCo particles capture microplastics at different concentrations.

GRAPHICAL ABSTRACT

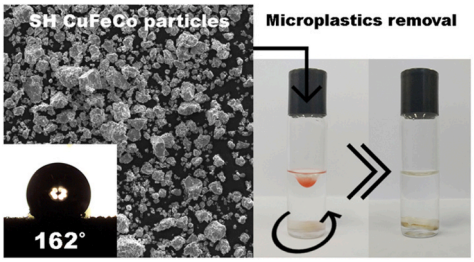

ARTICLE INFO

Keywords:
Superhydrophobic
Nanostructured
Mechanical alloying
Oil/water separation
Microplastics

ABSTRACT

A superhydrophobic CuFeCo powder alloy, obtained by combining high-energy ball milling (HEBM) and liquid phase deposition (LPD), was used to remove high-density polyethylene fibres from water. After 48 h of HEBM, CuFeCo solid solution powder with ferromagnetic properties was obtained. High-resolution transmission electron microscopy showed a crystallite size of 20 nm, confirming its nanostructure. The metallic CuFeCo powder surface was functionalised with dodecanoic acid to confer superhydrophobicity (water contact angle = 162 ± 1°) and superoleophilicity (oil contact angle ~ 0°). Taking advantage of its superwettable properties, superhydrophobic CuFeCo particles were used to capture microplastics (270 μm < size < 1240 μm), which is an innovative application of superhydrophobic materials. This study demonstrates an innovative way of using superhydrophobic materials in environmental applications such as the removal of solid pollutants like microplastics.

1. Introduction

An increasingly important issue in the 21st century is the emergence of microplastics (MP) as significant pollutants of natural waters compared to other types of pollutants such as heavy metals and oil spills. It is estimated that between 19 and 23 million metric tons of MPs were generated in 2016 around the globe, with this figure projected to reach up to 53 million metric tons by 2030 [1]. These solid pollutants directly affect the environment [2,3] and human health [4,5]. MPs are defined as solid polymers that present different chemical compositions and shapes, with a size smaller than five millimetres in length [6,7]. There are currently several methods available to remove MPs from water or waste water, such as electrocoagulation [8], air flotation [9], the use of filtration membranes [10], and the application of seagrass [11], among others [12]. There are also more innovative methods to remove MPs, such as the use of photocatalytic Au@Ni@TiO_2-based micromotors to

* Corresponding authors.
E-mail addresses: oriolriusayra@ub.edu (O. Rius-Ayra), abiserova.tahchieva@ub.edu (A. Biserova-Tahchieva).

https://doi.org/10.1016/j.colsurfa.2021.127075
Received 26 April 2021; Received in revised form 21 June 2021; Accepted 23 June 2021
Available online 7 July 2021

remove personal care products [13] and the application of a microfluidic device to sort and separate MPs *via* serial faradaic ion concentration polarisation. Furthermore, MP surfaces can be functionalised with hypochlorite (ClO^-) [14] or magnetite (Fe_3O_4) nanoparticles [15] to change their wettability properties and easily remove them by air flotation. Additionally, there are analytic methods used to separate MPs from aqueous solutions such as using castor oil [16] or canola oil [17].

Despite these processes, the use of membranes in the removal of MPs is gaining increasing attention because their production can be scaled up. Examples of the applications of such membranes include the use of polyacrylonitrile membranes in the removal of polystyrene spheres [18] and membrane bioreactors in the removal of MPs with an efficiency of 79.01% [19].

In the removal of different types of pollutants such as oils, superhydrophobic materials have shown promising results in separating oil from water when used in polymer membranes [20,21], metallic meshes [22,23] or sponges [24,25]. These systems have a water contact angle (WCA) $> 150°$, a sliding angle (SA) $< 10°$ and a contact angle hysteresis (CAH) $< 10°$ [26]. Moreover, if air is replaced by oil in the three-phase system (water-air-solid), the surface presents superoleophilicity under water, with an oil contact angle (OCA) close to 0° and rapid spreading that allows oil/water separation [27–29]. Despite the fact that these superwettable surfaces can remove immiscible pollutants, the actual challenge is to remove solid pollutants such as MPs. There are several methods that can be used to obtain superhydrophobic materials such as chemical etching [30,31], electrodeposition [32–34], sol-gel processes [35,36], hydrothermal processes [37,38] and liquid phase deposition (LPD) [39]. However, these are usually difficult to scale up and use in industrial applications. In this scenario, mechanical alloying (MA) or high-energy ball milling (HEBM) offers some advantages as they can produce large quantities of solid-state nanostructured materials with relatively simple equipment at room temperature and using a sustainable process [40–43].

Here, we report a superhydrophobic solid solution of CuFeCo alloy particles used to remove MPs. A nanostructured CuFeCo alloy with ferromagnetic properties was obtained using HEBM for 48 h. After that, the surface was functionalised by the LPD of dodecanoic acid (also known as lauric acid) in order to confer superhydrophobic and superoleophilic properties due to the intrinsically hydrophobic nature of the fatty acid. Taking advantage of their superwettable properties, particles of the CuFeCo alloy were used to capture MPs, demonstrating that superhydrophobic/superoleophilic materials can remove solid pollutants *via* the migration of MPs from water to the organic phase. This application of superhydrophobic materials opens up a new way to use these materials in the removal of solid pollutants.

2. Experimental procedure

2.1. Sample preparation

HEBM was carried out to obtain a nanostructured CuFeCo alloy using commercial powders of elementary Cu, Fe and Co (50:25:25 wt%). The metallic powder was milled at 300 rpm using a Pulverisette P6 high-energy planetary ball mill (from Fritsch) for different amounts of time (24 h, 36 h, 48 h and 96 h). To prevent oxidation, the experiment was carried out under an argon atmosphere ($>$ 99.9996%, purchased from Linde). High-strength steel balls (12 mm in diameter) were used at a ball-to-powder weight ratio of 20:1. LPD was carried out to confer superhydrophobicity to the ferromagnetic CuFeCo alloy. To prepare the superhydrophobic powder, 0.5 g of the mechanically alloyed powder was immersed in a solution of 0.3 M dodecanoic acid (99.8% extra pure) dissolved in synthesis-grade absolute ethanol (both purchased from Scharlab) for 24 h. Afterwards, the solid was washed several times with ethanol and dried in a fume hood.

2.2. Characterisation techniques

The morphology, composition and distribution of the processed powder grain sizes, as well as the changes at the surface of the particles produced by the dodecanoic acid functionalisation, were characterised. Phase evolution of the alloying process was measured with a PANalytical X'Pert Pro MPD θ/2θ Bragg-Brentano X-ray powder diffractometer (240 millimetres in radius) with Cu Kα radiation (1.5418 Å). Powder morphology was determined by a JEOL J-7100 field emission scanning electron microscope (FESEM) with an energy-dispersive X-ray spectroscopy (EDS) detector to assess element distribution and a backscattered electron (BSE) detector to observe the mean atomic number contrast. The particle-size distribution (PSD) of the CuFeCo particles was assessed by measuring the size of 200 particles in different FESEM micrographs and determining the particle size with ImageJ. High-resolution transmission electron microscopy (HR-TEM) was also used to confirm the crystal structures obtained from the X-ray studies. A JEOL JEM 2100 transmission electron microscope with an EDS detector and a Scanning Transmission Electron Microscope (STEM) annular dark field was used to characterise the nanostructure. The CaRIne and Gatan software was used to determine the planes as well as the crystallite size of the CuFeCo solid solution. High-resolution X-ray photoelectron spectroscopy (HR-XPS) was also used to determine chemical composition at the surface level with the PHI ESCA-5500 XPS system, using a monochromatic X-ray source (Kα(Al) = 1486.6 eV and 350 W). Spectral analysis was carried out with the MultiPak software. Infra-red spectroscopy was also undertaken to confirm the surface functionalisation, using attenuated total reflectance-Fourier transform infrared spectroscopy (ATR-FTIR; ABB Bomem FTLA) in the range of 4000–525 cm^{-1} at a resolution of 4 cm^{-1}. The magnetic properties of the powders were evaluated with the MPMS-XL superconducting quantum interference device (SQUID) magnetometer to evaluate the magnetic properties at 300 K. Brunauer–Emmett–Teller (BET) was applied to calculate the specific surface area and the pore size on the basis of nitrogen adsorption isotherm measurements at 77 K with a TriStar 3000 V 6.04 A in a relative pressure (P/P_0) range from 0.011 to 0.349. To measure the WCA, a Levenhuk DTX digital microscope was used with a 3.5 μL droplet of deionised water at room temperature. Mechanically alloyed CuFeCo particles were sprinkled over a flat surface containing an adhesive before being flattened by a glass slide in order to prevent roughness effects, with the excess powder removed thereafter [44]. The reported average of contact angle measurements were obtained by three repetitive measurements at different sites on the surface. To observe the morphology of the MPs before and after the separation process, a Motic reflected light microscope with white light was used. MP measurements were performed with the ImageJ software.

2.3. Oil/water separation

Oil/water separation was performed by adding the minimum mass of superhydrophobic CuFeCo particles to a glass vial containing 5 mL of deionised water until all the oil (stained with Oil Red O that was purchased from Scharlab) had been immediately adsorbed onto the metal. The oils used were hexane (synthesis grade; purchased from Scharlab), a mixture of o-, m- and p-xylene (synthesis grade; purchased from Alfa Aesar) and petroleum ether, boiling range 40–60 °C (environmental grade; purchased from Scharlab). The CuFeCo powder was added to the solution until it had adsorbed all the oil and the red colour was no longer observable. After that, a neodymium permanent magnet (13,000 Gauss) was used to separate the CuFeCo powder containing the oil from the water. Finally, the water was decanted, while the powder was rinsed in ethanol several times and dried in a fume hood. To recycle the CuFeCo particles so that they could be used again to remove oil, they were washed three times with absolute ethanol after each oil/water separation cycle and then dried in a fume hood for a few minutes until the ethanol had evaporated. The residual oil in water was determined by a

Levenhuk DTX digital microscope as well as the presence of Oil Red O. This oil/water separation process was of interest for the capture of MPs by the superhydrophobic CuFeCo particles.

2.4. Capture of microplastics

SiC P320 abrasive paper was used to grind high-density polyethylene (HDPE) pellets to obtain MP fibres (ranging from 270 μm to 1240 μm). Different concentrations of HDPE microfibres (ranging from 0.2 to 2.2 MP/mL) were added to a glass vial containing 5 mL of deionised water, which was then sonicated to heterogeneously distribute the fibres. After that, 50 μL of oil (hexane, xylene or petroleum ether) were poured into the glass vial containing the MPs, with the mixture under constant stirring and the MPs displaced to the bottom part of the vortex as a result of the centripetal force. The solvent did not partially dissolve the MPs or cause them to swell. The superhydrophobic CuFeCo particles (0.1 g) were added to the vial to capture the MPs. After that, a neodymium permanent magnet (13,000 Gauss) was used to retrieve the mixture of superhydrophobic CuFeCo particles, MPs and oil. Finally, under a magnetic field, the MPs were immobilised, and the aqueous phase was decanted to another vial and separated from the MPs, which were washed with absolute ethanol. The residual MP in water were determined by a Levenhuk DTX digital microscope as well as the presence of Oil Red O.

3. Results and discussion

3.1. Microstructural characterisation

FESEM was performed to determine the relationship between phase evolution and microstructural changes during the HEBM process. Moreover, EDS was carried out to determine the atomic distribution with milling time. Fig. 1 shows the evolution of particle morphology and size as a function of the milling time. Before HEBM, the particle morphology of the raw powder showed three different morphologies corresponding to Cu with a dendritic shape, Fe in perfect spheres and Co as platelets (Fig. 1S). The size of the particles decreased with the milling time. At short milling times, irregular shapes were more common and most of the particles were agglomerated (Fig. 1a). With longer milling times, the particle size was much smaller and more homogenous (Fig. 1c–d). For instance, particle sizes were around 10 ± 8 μm after 24 h of milling. After 48 h, there was no significant decrease in size, which was also the case after 96 h of milling (Fig. 1d). Semiquantitative EDS analysis of the CuFeCo powder milled for 48 h revealed characteristic Kα lines for Fe, Cu and Co of the solid solution at 6.398 eV, 8.040 eV and 6.924 eV, respectively (Figure S2).

HR-TEM was used to determine the crystal size, the nanostructure and also the unit cell obtained after HEBM. Fig. 2a depicts the nanostructure of the sample obtained after 48 h of milling, which was formed of crystals measuring around 20 nm [45,46]. In addition, the selected area electron diffraction (SAED) of this sample showed a ring patterning

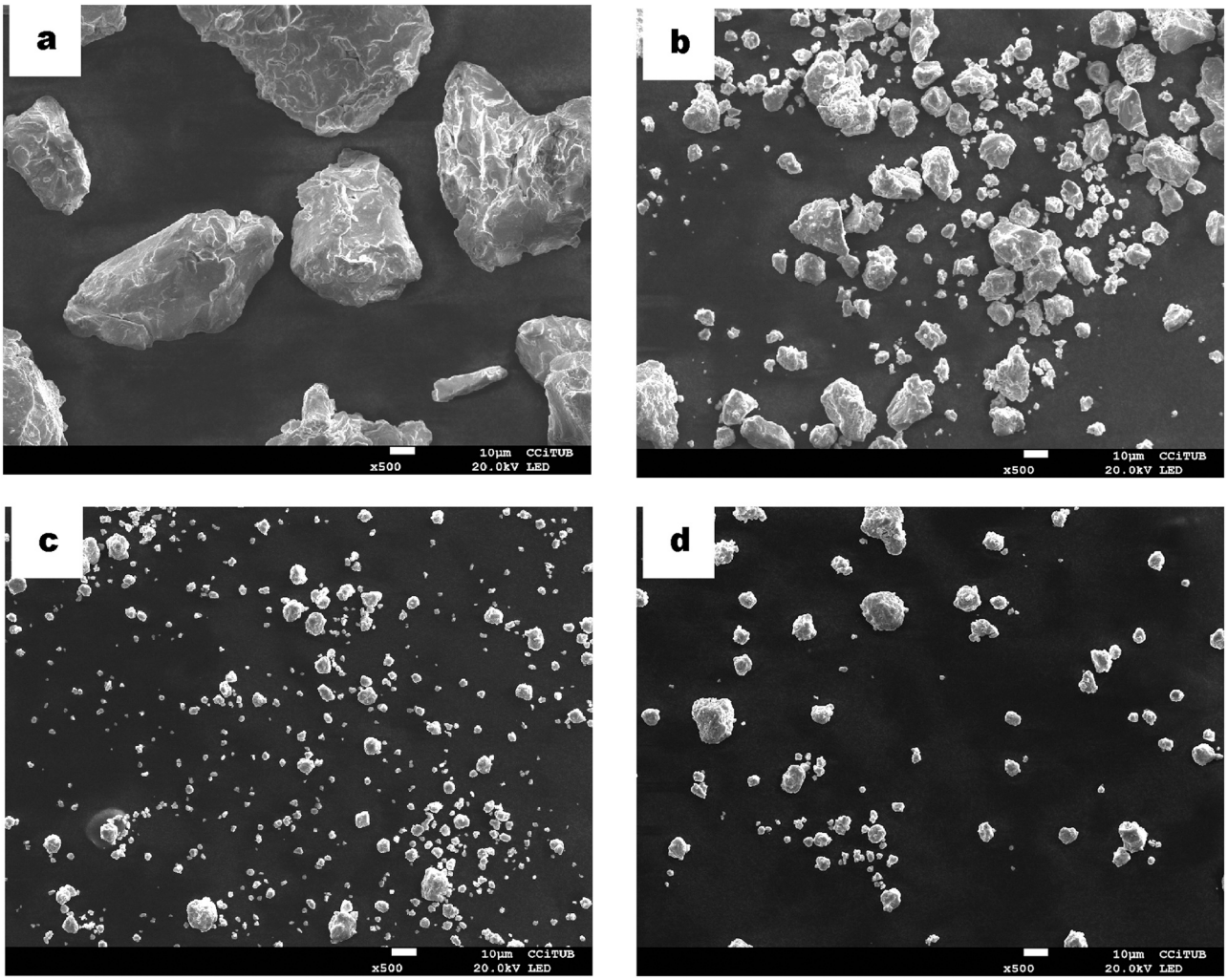

Fig. 1. FESEM micrographs of the CuFeCo particles milled for (a) 24 h, (b) 36 h, (c) 48 h and (d) 96 h.

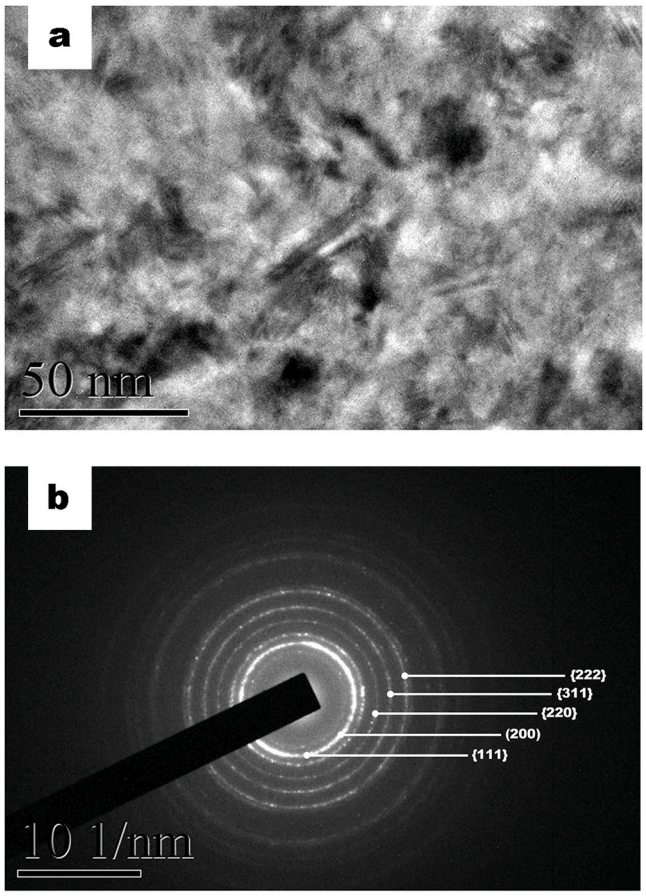

Fig. 2. HR-TEM images of a CuFeCo alloy sample obtained after 48 h of ball milling: (a) bright-field image showing crystals of around 20 nm and (b) SAED pattern that shows an fcc crystalline cell.

where five different planes could be identified: {111}, {200}, {220}, {311} and {222} corresponding to an fcc unit cell (Fig. 2b).

XRD confirmed that the CuFeCo solid solution powder had an fcc crystalline structure [46]. Fig. 3 shows the evolution of the CuFeCo powder composition initially and after different milling times. Initially, there were three different phases assigned to copper (fcc), where each peak corresponded to the planes {111}, {200}, {220}, {311} and {222}. For cobalt (fcc), the planes were assigned to {100}, {200}, {220} and {311}. Finally, in the case of iron (bcc), the assigned planes were {110}, {200}, {211} and {220}.

With increasing milling times, the peaks associated with Co and Fe showed reduced intensity and were no longer present after 24 h of milling. A peak broadening was also observed due to a reduction in the crystallite size, an accumulation of strain after each increase in milling time as well as instrumental broadening. During mechanical alloying, powder particles are forced to deform strongly through collisions with the milling media, being repeatedly deformed, cold-welded and fractured. Therefore, the density of defects, such as dislocations and vacancies, increases significantly, which increases atomic diffusion through the structure. In addition, refined microstructural features decrease the diffusion paths and promote atomic mobility. Continuous deformation severely distorts the unit cell structure. Thus, the slight shift in the 2θ position of the peaks observed in the XRD patterns (Fig. 3) was due to changes in the main lattice parameter. Ball milling produced a CuFeCo nanostructured powder alloy after 24 h of processing, which tended to decrease particle size as well as the crystallite size. This, in turn, led the Fe and Co atoms to be found in the Cu matrix, resulting in the whole fcc structure. These results indicated that ball milling caused the formation of a CuFeCo solid solution at room temperature in a homogenised way. Moreover, particle size after different ball milling times stabilised, with a plateau reached at 48 h of ball milling. These experimental conditions were selected to study the magnetic properties and surface functionalisation of the powder and its application in the capture of MPs.

3.2. Magnetic characterisation

The magnetic properties of the powder after milling were analysed under the same conditions (300 K). Fig. 4 shows the ferromagnetic behaviour of the unprocessed powder and the powder obtained after 48 h of milling. Hysteresis loops were observed, in which the magnetic saturation (M_s) of the raw powder was around 50 emu/g. All the mechanically alloyed powders presented ferromagnetic behaviour, notably the powder obtained after 48 h of milling that showed the best improvement in ferromagnetism (27 emu/g). Raw powder presented the highest saturation compared with the milled samples. This is because the M_s is strongly related to chemical composition rather than the microstructure of the system [40,47]. At the beginning, an inhomogeneous and disordered composition was present, and the magnetic properties of the Fe and Co atoms (the ones responsible for the magnetic behaviour) were not diluted by the Cu atoms, thus resulting in a significant M_S. With a prolonged milling time, the increase in M_S was due to the completion of alloying and a decrease in magnetocrystalline anisotropy caused by microstructure refinement, which led to an easier rotation of the magnetic vector [46].

Knowing that the magnetisation process originates through domain wall movement and spin rotation, it can thus be affected by crystallite refinement. When the crystallite size is of a few nanometres, each crystallite can be considered a single magnetic domain eliminating the influence of magnetic walls [46]. For smaller crystallites, ferromagnetic exchange interactions predominate, preventing the magnetic moments from aligning parallel to the easy axis of each individual crystallite. This results in a considerable reduction in magnetocrystalline anisotropy due to the averaging effect of magnetisation over randomly orientated nano-sized crystallites. Fig. 4 shows variations in the coercive field (H_c) before and after 48 h of milling. This parameter is structurally sensitive, and the changes are explained by the microstructural and compositional evolution. Coercivity increased from 25 emu/g for the initial powder to 50 emu/g after 48 h of milling due to the sharp reduction in the crystallite size (20 nm). In addition, it is known that for alloys with a large dislocation density, as observed in the case of the mechanically alloyed samples, H_c is dominated by the long-range residual stresses generated by dislocations [46].

3.3. Surface characterisation

ATR-FTIR spectroscopy allows the determination of the chemical composition of powder functionalised with dodecanoic acid [48,49]. Fig. 5 shows the spectra for the region between 4000 cm^{-1} and 1200 cm^{-1}, where the difference between the functionalised powder and pure dodecanoic acid can be clearly seen. In the case of pure dodecanoic acid, an intense and sharp band at *ca.* 1700 cm^{-1} was assigned to $\nu C{=}O$. By contrast, this band was not present in the spectrum for the functionalised powder, but a sharp and low intense band appeared at *ca.* 1580 cm^{-1} corresponding to $\nu_{as}COO^{-}$. Moreover, both spectra shared three different sharp and intense bands corresponding to the carbon chain appearing at *ca.* 2951 cm^{-1}, *ca.* 2911 cm^{-1} and *ca.* 2845 cm^{-1} and assigned to the alkyl chain stretching modes $\nu_{as}CH_3$, $\nu_{as}CH_2$ and $\nu_{s}CH_2$-CH_2, respectively. This difference between the two spectra allowed the identification of the presence of a carboxylate group on the metallic substrate. Additionally, the CuFeCo powder before milling and after LPD were also compared showing total absorbance.

The oxidation state as well as the chemical environment of the surface was determined using HR-XPS. Several peaks were identified in the spectra that were assigned to: C-1 s (285 eV), O-1 s (531 eV), Fe-2p3

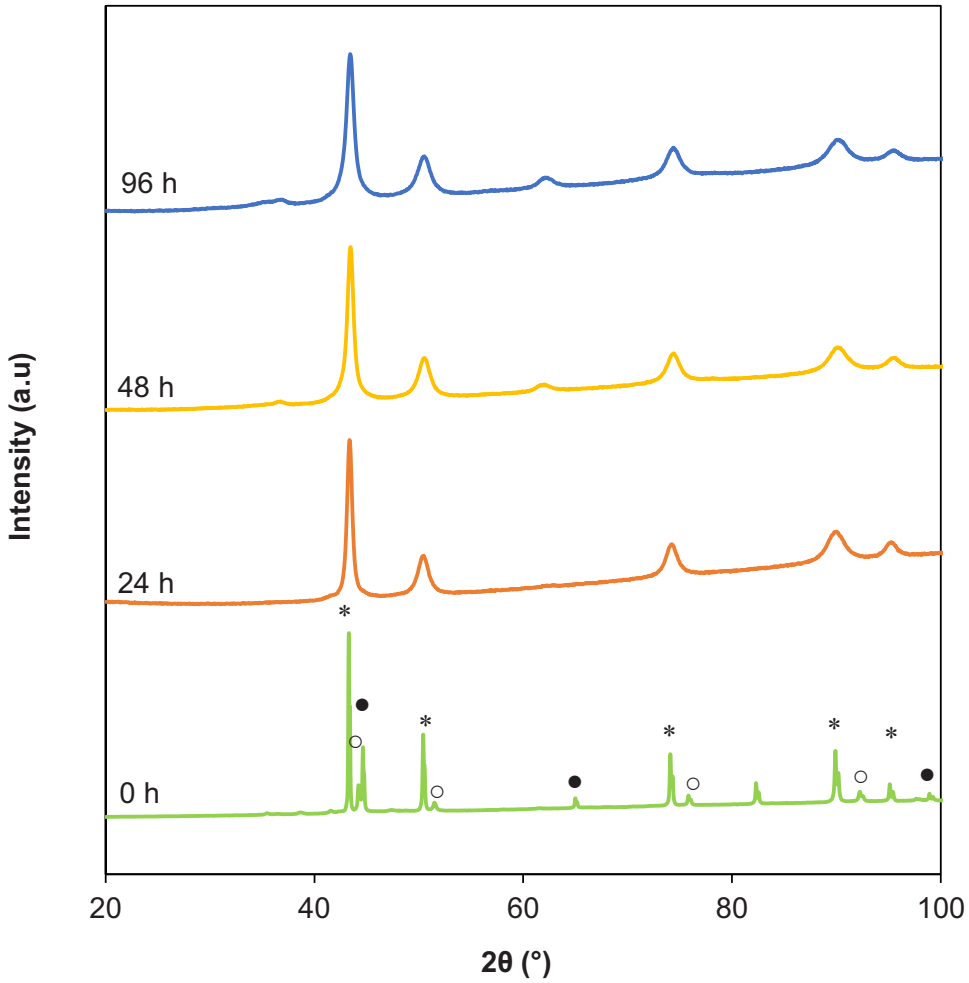

Fig. 3. XRD patterns for the CuFeCo composition initially and after different milling times (* for Cu, ○ for Co and • for Fe).

(712 eV), Co-2p3 (780 eV) and Cu-2p3 (934 eV). Their atomic percentages were also calculated (Table 1).

The HR-XPS spectrum of C-1s (Fig. 6a) showed two deconvolutions at 284.1 eV and 287.8 eV that were assigned to the C-C bond and carboxylate group (COO^-), respectively [50,51]. The O-1s peak (Fig. 6b) was also deconvoluted into three components: a peak at 529.6 eV corresponding to the oxygen-metal bond (O-M), a peak at 531.1 eV also corresponding to the oxygen-metal bond (O-M) and a peak at 532.2 eV corresponding to O-C. For the oxygen-metal bond deconvolutions, their chemical environment was assigned to α-FeOOH and $Co(OH)_2$, respectively [52,53]. Cu-2p showed four peaks (Fig. 6c) that were assigned to its spin orbit splitting and the corresponding shake-up satellites. The peaks at 933.8 eV and 942.3 eV corresponded to Cu-2p3/2 and its satellite, respectively, while the peaks at 953.5 eV and 962.3 eV were assigned to Cu-2p1/2 and its satellite, respectively, with the main sign of Cu-2p3/2 assigned to $Cu(OH)_2$ [52,54]. Fe-2p was deconvoluted into three peaks corresponding to the Fe (III) oxidation state (Fig. 6d). The peak at 712 eV was assigned to Fe-2p3/2, while the one at 723 eV corresponded to Fe-2p1/2. The peak at 717.9 eV was assigned to a shake-up satellite from the 2p3/2 contribution. The deconvolution of Fe-2p3/2 was assigned to the presence of α-FeOOH [53]. Finally, for Co-2p3 (Fig. 6e), the characteristic spin orbit splitting from the p orbitals was clearly observable in the spectra, with the peak at 780.3 eV corresponding to Co-2p3/2 and the peak at 795.8 eV assigned to Co-2p1/2. Moreover, the peaks at 785.3 eV and 802.8 eV corresponded to the shake-up satellites, respectively, with the main deconvolution of Co2p3/2 assigned to $Co(OH)_2$ [53,54].

Chemical characterisation was performed to determine the functionalisation of the CuFeCo ferromagnetic powder and changes in the wettability of the surface. Both ATR-FTIR and HR-XPS elucidate the presence of a carboxylate group (COO^-) in a functionalised surface derived from dodecanoic acid, confirming that during the LPD the fatty acid has reacted with the metallic surface to generate metal-dodecanoate all over the surface:

$$M^0/M-OH_{ads}+n \quad C_{11}H_{23}COOH \underset{EtOH}{\rightarrow} M(C_{11}H_{23}COO)_n+ \quad n{\cdot}H_2O \qquad (1)$$

where M = Co, Cu, Fe. Usually, metallic surfaces present hydroxyl groups adsorbed onto the surface that have an alkaline character. In LPD, carboxylic acid from the fatty acid reacts with these hydroxyl groups to produce metallic carboxylates, with the metals present in the solid solution. The presence of the carboxylate decreases the surface free energy of the system that, combined with the well-known hierarchical structure, confers superhydrophobic properties to the CuFeCo particles. This property is characteristic of a Cassie-Baxter state [55].

3.4. Wettable properties

As mentioned before, wettability is a key point when defining a surface as superhydrophobic. Thus, it is essential to measure its WCA. Before surface modification, the prepared CuFeCo powder showed hydrophilicity, with a WCA of $87 \pm 1°$ that indicated surface carbon contamination. After modification with dodecanoic acid, the WCA was $162 \pm 1°$ and the CAH was $1 \pm 1°$, indicating superhydrophobicity and low adhesion properties (Fig. 7a-b). The OCA was also measured using

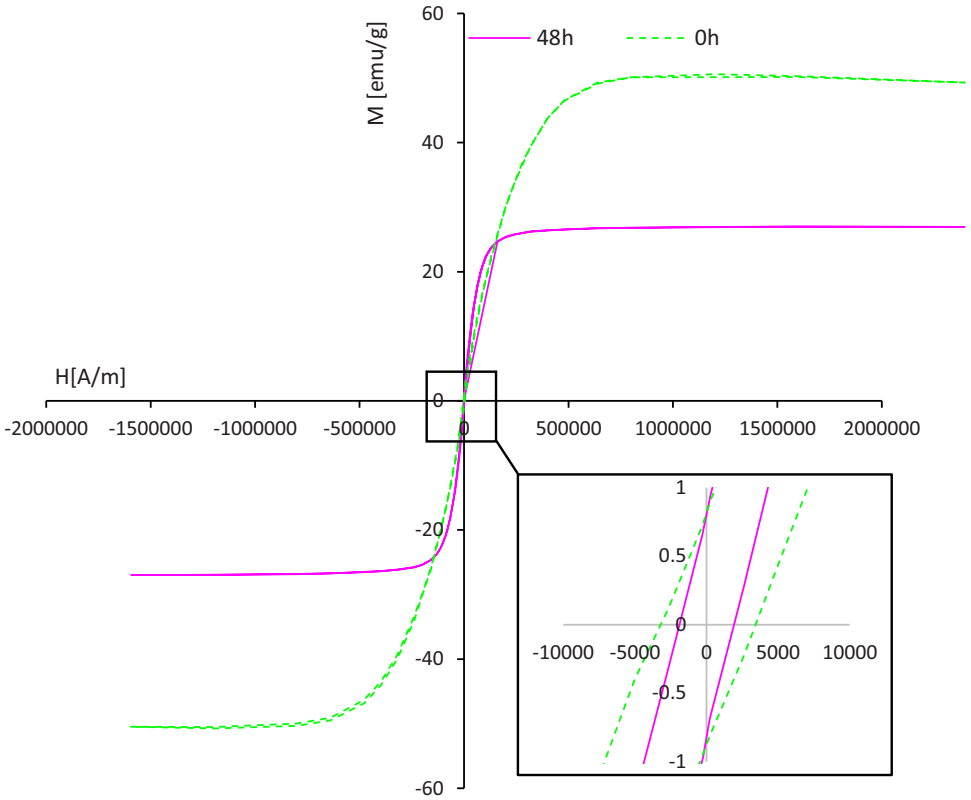

Fig. 4. Hysteresis loop of the unprocessed metallic powder (dotted line) and powder that was ball milled for 48 h (solid line).

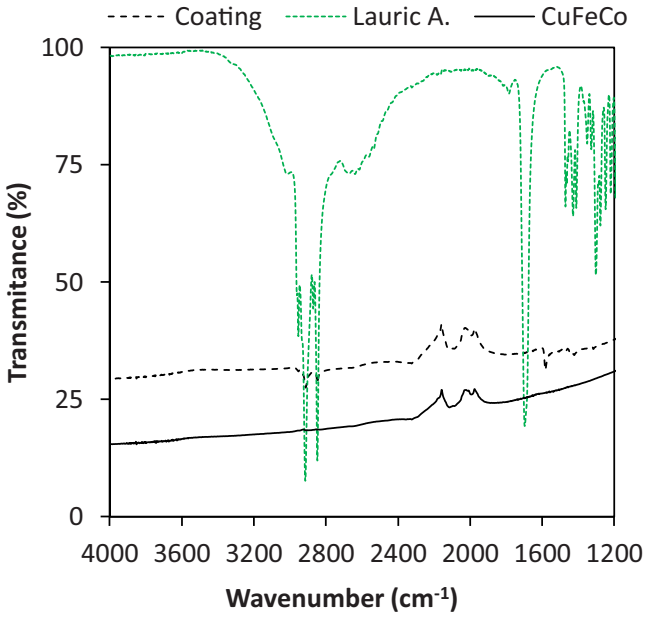

Fig. 5. ATR-FTIR spectroscopy shows the presence of a carboxylate group in the superhydrophobic CuFeCo powder surface (solid line) and pure dodecanoic acid (dotted line).

organic solvents (hexane, petroleum ether and xylene). Instantaneous and total oil adsorption was observed in all cases. Therefore, the OCA was ~ 0° (Fig. 7c). Another interesting and useful property of these systems is that they are superoleophilic under water when air is replaced by oil in the air-water-solid three-phase system.

It should be mentioned that the functionalised CuFeCo particles

Table 1
Atomic percentages for each element present in the HR-XPS spectra.

Element	Percentage (%)
C	65.8
O	22.8
Co	4.30
Fe	3.10
Cu	1.30

retained their superhydrophobicity (the WCA, SA, and CAH did not change) after one year of exposure to the environment, indicating excellent stability in atmospheric conditions. In addition, after 24 h in deionised water, the superhydrophobic CuFeCo powder was not oxidised and the WCA remained unaffected. Moreover, the durability of the particles was evaluated by placing them in contact with droplets of different pH values (pH = 1, 4, 7, 9, and 12) for 10 min. This test did not show any changes in the WCA, which was still higher than 150°, demonstrating excellent resistance against corrosive media. This also indicated that the particles were not oxidised and did not release copper, iron or cobalt ions into the aqueous solution.

Since superhydrophobic surfaces can be superoleophilic under water, it was important to determine the underwater oil contact angle (UWOCA) of the superhydrophobic CuFeCo powder. Assuming a flat surface, the UWOCA can be expressed by the Bartell-Osterhof equation (Eq. 2) as follows:

$$cos\theta_{ow} = \frac{\gamma_{oa} cos\theta_0 - \gamma_{wa} cos\theta_w}{\gamma_{ow}} \quad (2)$$

where θ_{ow}, θ_w and θ_o are the UWOCA, the static WCA and the static OCA, respectively, while γ_{oa}, γ_{wa} and γ_{ow} represent the surface free energy of oil-air, water-air and oil-water, respectively. Considering the hexane-water interfacial tension (γ_{ow} = 50.25 mN/m), the xylene-water

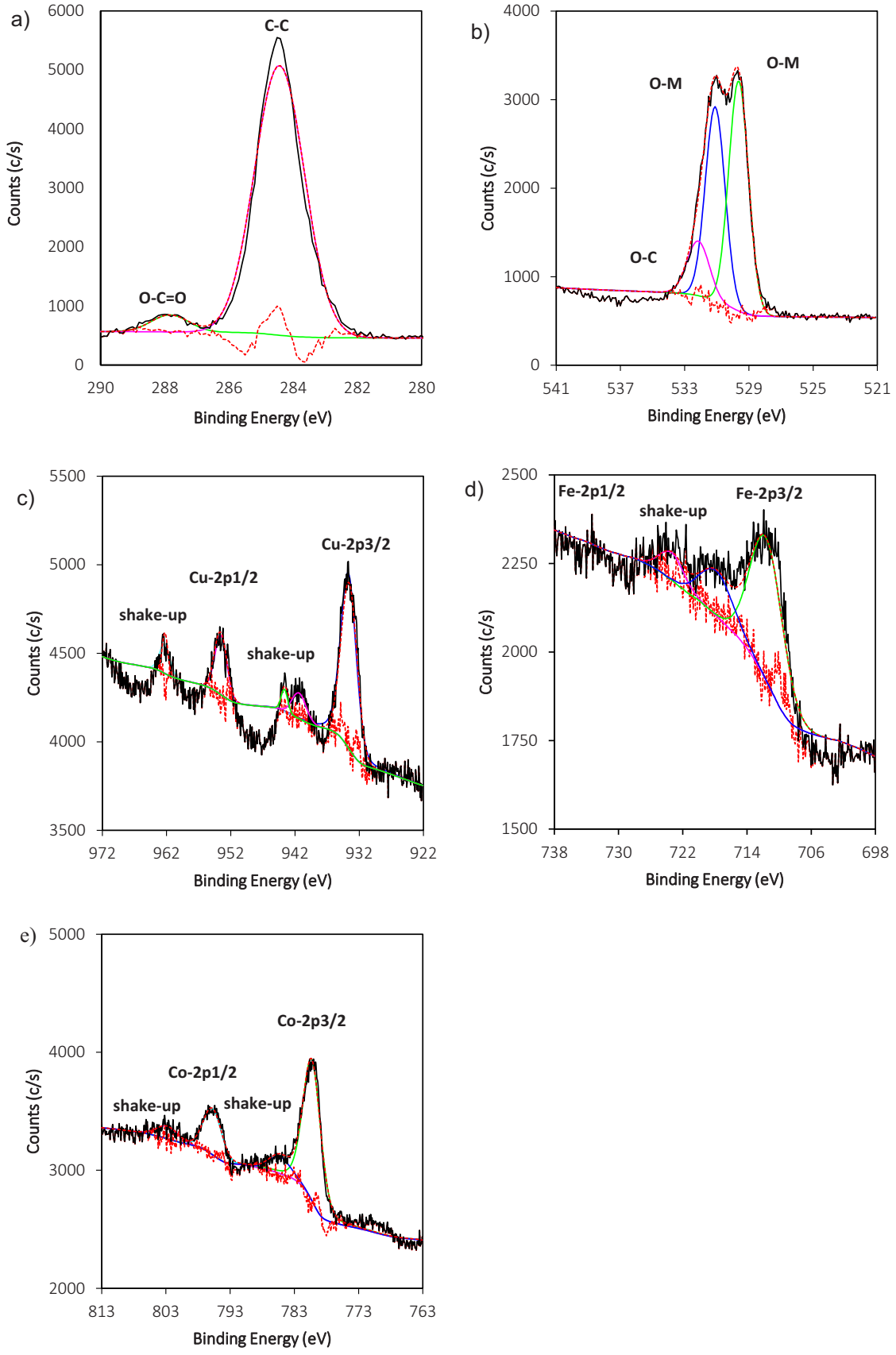

Fig. 6. HR-XPS of the chemical state of the metals in the nanocrystalline powder and the presence of a carboxylate group between oxygen and the metals: (a) C-1s; (b) O-1s; (c) Cu-2p; (d) Fe-2p and (e) Co-2p.

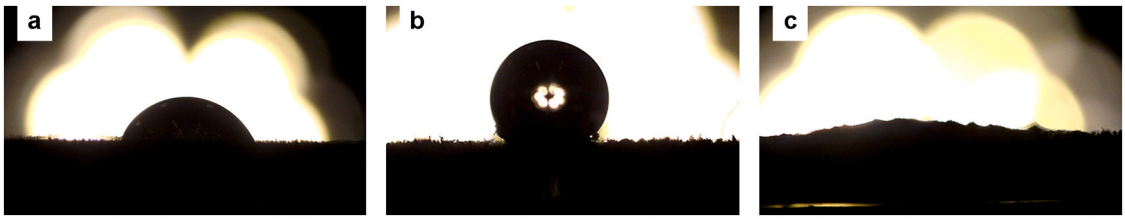

Fig. 7. Images of contact angles measurements: (a) before modification, the surface exhibited a WCA of 87 ± 1°; (b) after modification with dodecanoic acid, the WCA was 162 ± 1° and (c) total adsorption of oil produces an OCA ~ 0°.

interfacial tension (γ_{ow} = 33.40 mN/m), the surface free energy of hexane-air (γ_{oa} = 18.43 mN/m), the surface free energy of xylene-air (γ_{oa} = 29.50 mN/m) and the surface free energy of water-air (γ_{wa} = 72.0 mN/m), the calculated values of θ_{ow} for hexane and xylene were 1.5° and 1.6°, respectively. These results confirmed that the surface was highly superoleophilic under water and allowed the separation of oil from water.

Oil/water separation was carried out by pouring the minimum amount of CuFeCo particles into the two-phase system (Fig. 8, left vial). The oil was adsorbed onto the powder surface and a characteristic marble was formed, indicating that the sorption process was occurring (Fig. 8, middle vial) [28]. Given the ferromagnetic properties of the CuFeCo powder, a permanent magnet was used once all the oil had been adsorbed onto the surface to separate the oil-solid system from the water. Thus, pure water without the presence of oil or solid particles was obtained (Fig. 8, right vial). Different volumes of hexane, petroleum ether and xylene (40 μL, 80 μL, and 120 μL) were used with deionised water to study oil/water separation. First, the minimum amount of CuFeCo particles was added until a marble was formed, depending on the volume and the organic solvent used. This marble is characteristic of the oil/water separation process [56]. Then, a neodymium permanent magnet was used to retrieve the superhydrophobic CuFeCo particles containing the oil, while the water was decanted. This process was repeated up to 10 times before the powder lost its superhydrophobicity (WCA < 150°). The separation efficiency remained constant after each cycle.

Fig. 8. Oil/water separation involving three stages: left, the water and oil (red) phases; middle, the addition of the minimum quantity of superhydrophobic CuFeCo powder that leads to the formation of an oil-containing marble; and right, pure water without oil.

The separation efficiency and sorption capacity were calculated using Eqs. (3) and (4), respectively:

$$\eta = V/V_o.100 \quad (3)$$

$$Q = (m_e - m_o)/m_o.100 \quad (4)$$

where V is the water volume after the separation and V_o the volume of oil and water before the separation in Eq. (3), and m_o is the mass of CuFeCo particles before the adsorption and me the total mass of powder and oil after the process in Eq. (4). The separation efficiencies were 97.0%, 96.5% and 96.0% and the sorption capacities were 82.0%, 60.0% and 40.0% for hexane, petroleum ether and xylene, respectively (Table 2).

These results revealed that different amounts of the CuFeCo solid solution powder were required to adsorb 40 μL of each oil due to the different viscosities of the oils [57–59]. Since hexane has the lowest viscosity (0.3 mPa·s) among the oils tested in this study, it required more CuFeCo particles for adsorption than petroleum ether (0.4 mPa·s) and xylene, which has the highest viscosity (0.8 mPa·s). The minimum mass of CuFeCo particles used to remove 40 μL, 80 μL and 120 μL of each type of oil were, respectively: 108.9 ± 1 mg, 179.2 ± 3 mg and 309.2 ± 5 mg for hexane; 118.6 ± 2 mg, 172.3 ± 2 mg and 196.9 ± 3 mg for the xylene isomers; and 121.5 ± 2 mg, 118.2 ± 2 mg and 146.4 ± 3 mg for petroleum ether. Since the superhydrophobic CuFeCo particles are homogeneous in their surface chemical composition as well as morphology and hierarchical structure, it is the viscosity of each oil that reduces the penetration into the structure and, therefore, the oil holding capacity. Accordingly, as the viscosity increases from hexane to xylene, the sorption capacity decreases. Additionally, the specific surface area as well as the pore size were also evaluated resulting in 0.7507 m^2/g and pore width was 15 Å, respectively. The N_2 adsorption/desorption curves for the superhydrophobic CuFeCo samples are presented in Figure S3.

3.5. Capture of microplastics

Once it was demonstrated that the CuFeCo particles could separate oil from water, the ability of the superhydrophobic CuFeCo powder to remove MPs was studied. Different amounts of HDPE-MPs (0.2 MP/mL, 0.6 MP/mL, 1.0 MP/mL, 1.4 MP/mL, 1.8 MP/mL and 2 MP/mL) were used. Three oils with different viscosities were used: hexane, petroleum ether and xylene. It is important to note that the method described in Section 2.4 caused the MPs to be displaced from the aqueous phase to the organic phase, indicating that the HDPE-MPs had better affinity for oils than for water. After adding 0.1 g of the superhydrophobic CuFeCo powder to the vortex (Fig. 9a) and under stirring conditions, a constant

Table 2
Average separation efficiency (η) and sorption capacity (Q) of the solid particles.

	Hexane	Petroleum ether	Xylene
η (%)	97.0 ± 1	96.5 ± 2	96.0 ± 2
Q (%)	82.0 ± 2	60.0 ± 5	40.0 ± 4

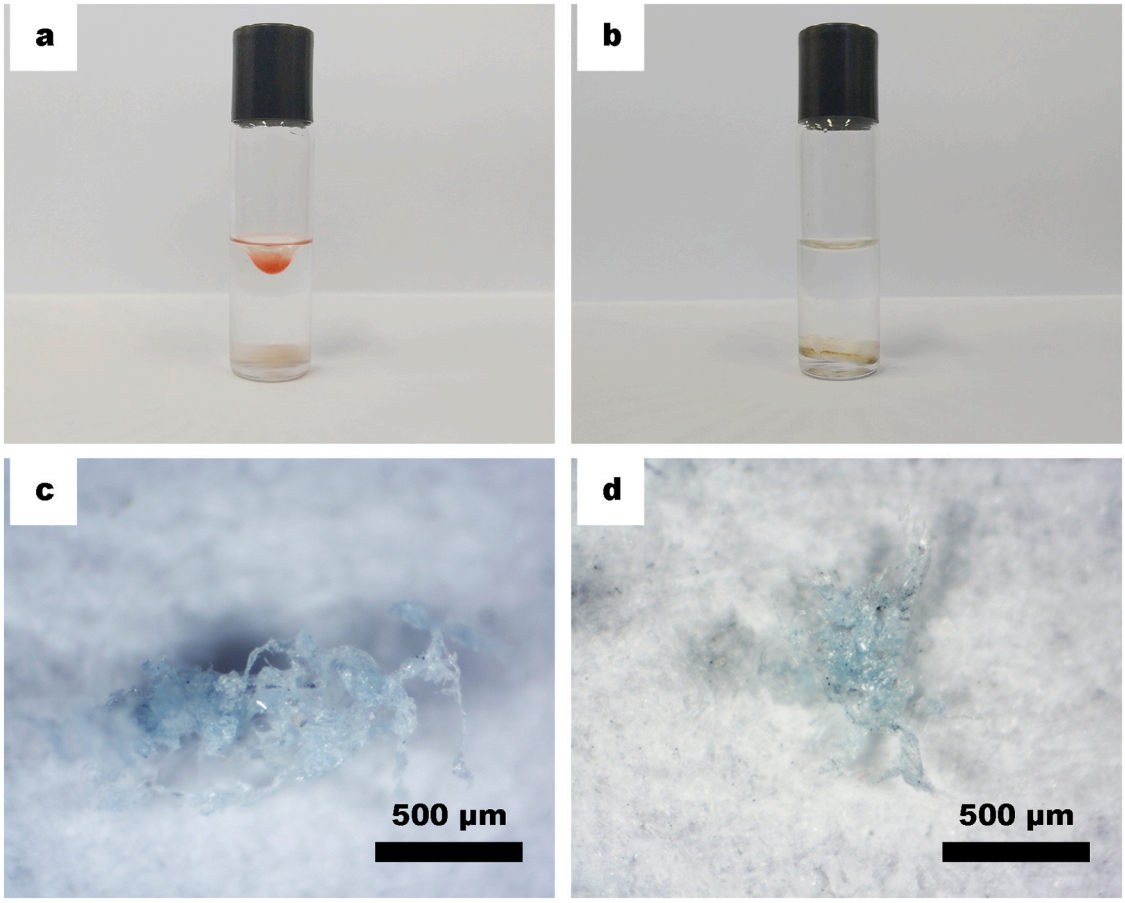

Fig. 9. Two different stages of the MP removal experiment using the CuFeCO powder: (a) under constant stirring, MPs were displaced from the water to the oil (red) in the stirring vortex before the superhydrophobic CuFeCo powder was added to the vortex and (b) water without the presence of MPs or hexane. Optical microscopy images of MPs (c) showing an irregular morphology before the capture experiment, and (d) exhibiting a more rounded morphology after the experiment.

magnetic field was applied using a neodymium permanent magnet to retrieve the CuFeCo particles with the attached MPs and organic solvent. Once the MPs were attracted to the magnetic field and immobilised, the water without the oil and MPs was decanted to another vial (Fig. 9b and Video S1). Finally, the vial containing the CuFeCo particles, MPs and the organic phase was washed with absolute ethanol. It should be noted that the morphology as well as the size of the MPs varied slightly after their removal using this method. In fact, as seen in Fig. 9c and d, the MPs had an irregular morphology before the removal process and a more rounded morphology after the process. This difference was due to the stirring process that induced a reorganisation of the MPs. Moreover, the size of the MPs decreased by nearly 30%, although the MPs were not broken down. Finally, the CuFeCo powder was recycled up to ten times without losing its superhydrophobicity or releasing metallic ions (Fe, Co or Cu). To recycle the CuFeCo powder, the powder was first washed with ethanol to remove the oil. Second, a small quantity of deionised water was added and the mixture was sonicated to detach the MPs from the particles. Finally, the CuFeCo solid solution was retrieved under a magnetic field and the water containing the collected MPs was decanted.

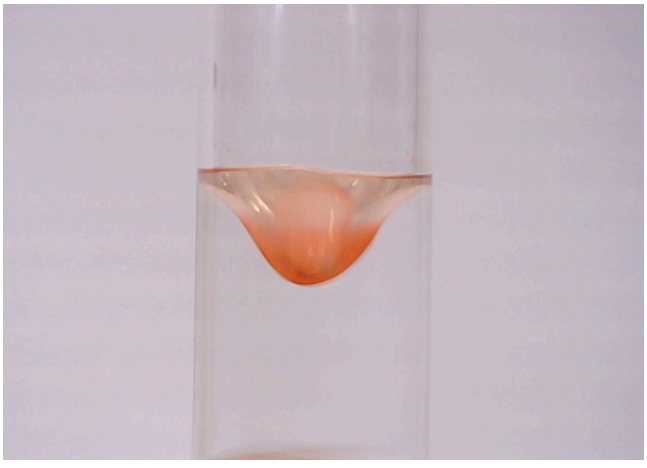

Video 1. A video clip is available online. Supplementary material related to this article can be found online at doi:10.1016/j.colsurfa.2021.127075.

The recovered MPs were quantified, and the capture efficiency (ξ) and the efficiency of the process (η) were calculated as follows:

$$\xi(\%) = C_{0,MP}/C_{MP}.100 \quad (5)$$

$$\eta(\%) = m_{0,MP}/m_{MP}.100 \quad (6)$$

where $C_{0,MP}$ and C_{MP} are the concentration of the MP (MP/mL) before and after the capture, respectively, while $m_{0,MP}$ and m_{MP} are the mass of MPs before and after the process, respectively. As shown in

Table 3
Concentrations of the MPs during the capture test, the capture efficiency (ξ) and the efficiency of the process (η).

$C_{0,MP}$	C_{MP}	ξ (%)	η (%)
0.2	0.2 ± 0.1	100 ± 1	100 ± 1
0.6	0.6 ± 0.1	100 ± 1	100 ± 1
1.0	1.0 ± 0.1	100 ± 1	100 ± 1
1.4	1.7 ± 0.1	83.0 ± 0.1	100 ± 1
1.8	2.1 ± 0.1	87.5 ± 0.1	100 ± 1
2.2	2.4 ± 0.2	90.2 ± 0.2	100 ± 1

Table 3, the capture efficiency reached its highest values at lower MP concentrations, indicating that the CuFeCo powder captured the MPs. By contrast, the capture efficiency decreased slightly at higher concentrations. The decrease in concentration was due to the decrease in the absolute number of the MPs caused by agglomeration during stirring. Additionally, the efficiency of the process, which depended on the MP mass and was therefore not affected by agglomeration, showed values of 100%, confirming that all the MPs had been captured and removed efficiently from the solution.

The capture process was based on three combined mechanisms: the migration of MPs from water to the organic phase that was a hydrophobic solvent, the ability of oil to permeate the surface of the CuFeCo particles due to their superhydrophobic/superoleophilic properties and the ability of the CuFeCo particles to easily move and adapt to the shape of the MPs. Thus, MP capture can be described as follows. Once the oil has been added and under constant stirring, the MPs are displaced from water to the organic phase in the stirring vortex. After the addition of the superhydrophobic CuFeCo particles to the stirring vortex, the particles are immediately displaced from the aqueous phase to the organic one, which is the oil, because of better affinity. In the presence of the organic solvent, the superhydrophobic CuFeCo particles start to form the characteristic marble and, enhanced by the centripetal force of the stirring process, the particles surround the MPs in the organic phase in order to capture them. As the CuFeCo particles are 20 times smaller than the MPs, they completely surround the MPs and capture them. Finally, a neodymium permanent magnet is used to retrieve the CuFeCo particles containing the attached MPs, while the water without any oil or MPs is decanted.

4. Conclusions

Nanostructured superhydrophobic CuFeCo alloyed particles were obtained to capture and remove microplastics. First, high-energy ball milling was used to prepare the CuFeCo solid solution. The liquid phase deposition of dodecanoic acid was then carried out to functionalise the surface and confer superhydrophobicity. FESEM revealed a decrease in the CuFeCo particle size to 10 μm after 24 h of milling, while HR-TEM showed a crystallite size of 20 nm. SQUID analysis confirmed the soft ferromagnetic properties of the CuFeCo particles, which was then used to retrieve these particles containing the oil (hexane, petroleum ether or xylene) and MPs by applying an external magnetic field. HR-XPS and ATR-FTIR analyses indicated surface functionalisation of the CuFeCo particles with a metal-dodecanoate compound, which caused a decrease in the surface free energy and an increase in the contact angle that indicated superhydrophobicity (WCA $= 162 \pm 1^{\circ}$ and CAH $= 1 \pm 1^{\circ}$) and superoleophilicity (OCA $\sim 0^{\circ}$). Finally, by taking advantage of these superwettable properties, the superhydrophobic CuFeCo particles were used to capture and remove HDPE-MPs at different concentrations with a capture efficiency (ξ) $> 83\%$. The mass of MPs did not change, showing an efficiency of the process (η) of 100%. This process involved the migration of MPs from water to the organic phase (hexane, petroleum ether or xylene) and the ability of the metallic particles to easily adapt to and surround the MPs. The application of an external magnetic field enabled the retrieval of the CuFeCo particles along with the attached MPs and the organic phase, leaving no MPs in the water phase.

Superhydrophobic materials have been widely used to remove organic solvents, but their ability to remove solid pollutants such as microplastics remains a challenge. Here, we report that these materials can be effectively used to remove microplastics. Moreover, we used a straightforward method that can be used in water treatment plants to remove pollutants such as oils and microplastics under constant stirring. Thus, this study provides a new environmental application of superhydrophobic materials in the removal of microplastics.

Funding

This research did not receive any specific grant from funding agencies in the public, commercial, or not-for-profit sectors.

CRediT authorship contribution statement

O. Rius-Ayra: Conceptualisation, Validation, Methodology, Investigation, Data Curation, Writing – original draft, Writing – review & editing, Visualization, Supervision. **A. Biserova-Tahchieva:** Conceptualisation, Validation, Methodology, Investigation, Data curation, Writing – original draft, Writing – review & editing, Visualization. **I. Lopez-Jimenez:** Conceptualisation, Validation, Methodology, Investigation, Data curation, Writing – original draft. **N. Llorca-Isern:** Conceptualisation, Validation, Methodology, Investigation, Data curation, Writing – original draft, Writing – review & editing, Funding acquisition.

Declaration of Competing Interest

The authors declare that they have no known competing financial interests or personal relationships that could have appeared to influence the work reported in this paper.

References

[1] S.B. Borrelle, J. Ringma, K.L. Law, C.C. Monnahan, L. Lebreton, A. McGivern, E. Murphy, J. Jambeck, G.H. Leonard, M.A. Hilleary, M. Eriksen, H.P. Possingham, H. De Frond, L.R. Gerber, B. Polidoro, A. Tahir, M. Bernard, N. Mallos, M. Barnes, C.M. Rochman, Predicted growth in plastic waste exceeds efforts to mitigate plastic pollution, Science 80 (369) (2020) 1515–1518, https://doi.org/10.1126/science.aba3656.

[2] Y. Zhang, S. Kang, S. Allen, D. Allen, T. Gao, M. Sillanpää, Atmospheric microplastics: a review on current status and perspectives, Earth-Sci. Rev. 203 (2020), 103118, https://doi.org/10.1016/j.earscirev.2020.103118.

[3] S. Xu, J. Ma, R. Ji, K. Pan, A.-J. Miao, Microplastics in aquatic environments: occurrence, accumulation, and biological effects, Sci. Total Environ. 703 (2020), 134699, https://doi.org/10.1016/j.scitotenv.2019.134699.

[4] J.C. Prata, J.P. da Costa, I. Lopes, A.C. Duarte, T. Rocha-Santos, Environmental exposure to microplastics: an overview on possible human health effects, Sci. Total Environ. 702 (2020), 134455, https://doi.org/10.1016/j.scitotenv.2019.134455.

[5] R. Zhou, G. Lu, Z. Yan, R. Jiang, X. Bao, P. Lu, A review of the influences of microplastics on toxicity and transgenerational effects of pharmaceutical and personal care products in aquatic environment, Sci. Total Environ. 732 (2020), 139222, https://doi.org/10.1016/j.scitotenv.2020.139222.

[6] L.S. Fendall, M.A. Sewell, Contributing to marine pollution by washing your face: microplastics in facial cleansers, Mar. Pollut. Bull. 58 (2009) 1225–1228, https://doi.org/10.1016/j.marpolbul.2009.04.025.

[7] S. Ziajahromi, P.A. Neale, F.D.L. Leusch, Wastewater treatment plant effluent as a source of microplastics: review of the fate, chemical interactions and potential risks to aquatic organisms, Water Sci. Technol. 74 (2016) 2253–2269, https://doi.org/10.2166/wst.2016.414.

[8] W. Perren, A. Wojtasik, Q. Cai, Removal of microbeads from wastewater using electrocoagulation, ACS Omega 3 (2018) 3357–3364, https://doi.org/10.1021/acsomega.7b02037.

[9] J. Talvitie, A. Mikola, A. Koistinen, O. Setälä, Solutions to microplastic pollution – Removal of microplastics from wastewater effluent with advanced wastewater treatment technologies, Water Res 123 (2017) 401–407, https://doi.org/10.1016/j.watres.2017.07.005.

[10] L. Li, G. Xu, H. Yu, J. Xing, Dynamic membrane for micro-particle removal in wastewater treatment: performance and influencing factors, Sci. Total Environ. 627 (2018) 332–340, https://doi.org/10.1016/j.scitotenv.2018.01.239.

[11] A. Sanchez-Vidal, M. Canals, W.P. de Haan, J. Romero, M. Veny, Seagrasses provide a novel ecosystem service by trapping marine plastics, Sci. Rep. 11 (2021) 254, https://doi.org/10.1038/s41598-020-79370-3.

[12] M. Enfrin, L.F. Dumée, J. Lee, Nano/microplastics in water and wastewater treatment processes – Origin, impact and potential solutions, Water Res. 161 (2019) 621–638, https://doi.org/10.1016/j.watres.2019.06.049.

[13] L. Wang, A. Kaeppler, D. Fischer, J. Simmchen, Photocatalytic TiO 2 micromotors for removal of microplastics and suspended matter, ACS Appl. Mater. Interfaces 11 (2019) 32937–32944, https://doi.org/10.1021/acsami.9b06128.

[14] J. Wang, D. Yue, H. Wang, In situ Fe3O4 nanoparticles coating of polymers for separating hazardous PVC from microplastic mixtures, Chem. Eng. J. 407 (2021), 127170, https://doi.org/10.1016/j.cej.2020.127170.

[15] J. Wang, H. Wang, D. Yue, Insights into mechanism of hypochlorite-induced functionalization of polymers toward separating BFR-containing components from microplastics, ACS Appl. Mater. Interfaces 12 (2020) 36755–36767, https://doi.org/10.1021/acsami.0c09586.

[16] T. Mani, S. Frehland, A. Kalberer, P. Burkhardt-Holm, Using castor oil to separate microplastics from four different environmental matrices, Anal. Methods 11 (2019) 1788–1794, https://doi.org/10.1039/C8AY02559B.
[17] E.M. Crichton, M. Noël, E.A. Gies, P.S. Ross, A novel, density-independent and FTIR-compatible approach for the rapid extraction of microplastics from aquatic sediments, Anal. Methods 9 (2017) 1419–1428, https://doi.org/10.1039/C6AY02733D.
[18] R. Wang, L. Zhang, B. Chen, X. Zhu, Low-pressure driven electrospun membrane with tuned surface charge for efficient removal of polystyrene nanoplastics from water, J. Membr. Sci. 614 (2020), 118470, https://doi.org/10.1016/j.memsci.2020.118470.
[19] J. Bayo, J. López-Castellanos, S. Olmos, Membrane bioreactor and rapid sand filtration for the removal of microplastics in an urban wastewater treatment plant, Mar. Pollut. Bull. 156 (2020), 111211, https://doi.org/10.1016/j.marpolbul.2020.111211.
[20] J. Zhang, Q. Xue, X. Pan, Y. Jin, W. Lu, D. Ding, Q. Guo, Graphene oxide/polyacrylonitrile fiber hierarchical-structured membrane for ultra-fast microfiltration of oil-water emulsion, Chem. Eng. J. 307 (2017) 643–649, https://doi.org/10.1016/j.cej.2016.08.124.
[21] Z. Wang, X. Jiang, X. Cheng, C.H. Lau, L. Shao, Mussel-inspired hybrid coatings that transform membrane hydrophobicity into high hydrophilicity and underwater superoleophobicity for oil-in-water emulsion separation, ACS Appl. Mater. Interfaces 7 (2015) 9534–9545, https://doi.org/10.1021/acsami.5b00894.
[22] H. Zhu, D. Chen, N. Li, Q. Xu, H. Li, J. He, J. Lu, Dual-layer copper mesh for integrated oil-Water separation and water purification, Appl. Catal. B Environ. 200 (2017) 594–600, https://doi.org/10.1016/j.apcatb.2016.07.028.
[23] X. Chen, Y. He, Y. Fan, Q. Yang, X. Yang, G. Zeng, L. Zhang, A smart engineering material with UV-induced switchable wettability for controllable oil/water separation, J. Chem. Technol. Biotechnol. 93 (2018) 476–488, https://doi.org/10.1002/jctb.5378.
[24] Q. Zhu, Q. Pan, F. Liu, Facile removal and collection of oils from water surfaces through superhydrophobic and superoleophilic sponges, J. Phys. Chem. C. 115 (2011) 17464–17470, https://doi.org/10.1021/jp2043027.
[25] Z. Xu, Y. Zhao, H. Wang, X. Wang, T. Lin, A superamphiphobic coating with an ammonia-triggered transition to superhydrophilic and superoleophobic for oil-water separation, Angew. Chem. Int. Ed. 54 (2015) 4527–4530, https://doi.org/10.1002/anie.201411283.
[26] B. Bhushan, Y.C. Jung, Natural and biomimetic artificial surfaces for superhydrophobicity, self-cleaning, low adhesion, and drag reduction, Prog. Mater. Sci. 56 (2011) 1–108, https://doi.org/10.1016/j.pmatsci.2010.04.003.
[27] M. Liu, S. Wang, L. Jiang, Nature-inspired superwettability systems, Nat. Rev. Mater. 2 (2017) 17036, https://doi.org/10.1038/natrevmats.2017.36.
[28] S. Nagappan, C.S. Ha, Emerging trends in superhydrophobic surface based magnetic materials: Fabrications and their potential applications, J. Mater. Chem. A 3 (2015) 3224–3251, https://doi.org/10.1039/c4ta05078a.
[29] Z. Chu, Y. Feng, S. Seeger, Oil/water separation with selective superantiwetting/superwetting surface materials, Angew. Chem. Int. Ed. 54 (2015) 2328–2338, https://doi.org/10.1002/anie.201405785.
[30] J. Brassard, J. Laforte, C. Blackburn, J. Perron, D.K. Sarkar, Silicone based superhydrophobic coating efficient to reduce ice adhesion and accumulation on aluminum under offshore arctic conditions, Ocean Eng. 144 (2017) 135–141, https://doi.org/10.1016/J.OCEANENG.2017.08.022.
[31] A.M. Escobar, N. Llorca-Isern, Superhydrophobic coating deposited directly on aluminum, Appl. Surf. Sci. 305 (2014) 774–782, https://doi.org/10.1016/j.apsusc.2014.03.196.
[32] A.M. Escobar, N. Llorca-Isern, O. Rius-Ayra, Identification of the mechanism that confers superhydrophobicity on 316L stainless steel, Mater. Charact. 111 (2016) 162–169, https://doi.org/10.1016/j.matchar.2015.11.026.
[33] Z. Chen, L. Hao, M. Duan, C. Chen, Electrodeposition fabrication of Co-based superhydrophobic powder coatings in non-aqueous electrolyte, Appl. Phys. A Mater. Sci. Process. 111 (2013) 581–585, https://doi.org/10.1007/s00339-012-7263-1.
[34] N. Llorca-Isern, A.M. Escobar, O. Rius, Scalable methods to obtain superhydrophobicity onto metallic surface, Mater. Sci. Forum 879 (2016) 2501–2506, https://doi.org/10.4028/www.scientific.net/MSF.879.2501.
[35] S. Foorginezhad, M.M. Zerafat, Fabrication of stable fluorine-free superhydrophobic fabrics for anti-adhesion and self-cleaning properties, Appl. Surf. Sci. 464 (2019) 458–471, https://doi.org/10.1016/j.apsusc.2018.09.058.
[36] D. Lin, X. Zeng, H. Li, X. Lai, T. Wu, One-pot fabrication of superhydrophobic and flame-retardant coatings on cotton fabrics via sol-gel reaction, J. Colloid Interface Sci. 533 (2019) 198–206, https://doi.org/10.1016/j.jcis.2018.08.060.
[37] W. Zhou, S. Li, Y. Liu, Z. Xu, S. Wei, G. Wang, J. Lian, Q. Jiang, Dual superlyophobic copper foam with good durability and recyclability for high flux, high efficiency, and continuous oil-water separation, ACS Appl. Mater. Interfaces 10 (2018) 9841–9848, https://doi.org/10.1021/acsami.7b19853.
[38] Z. Kang, J. Zhang, L. Niu, A one-step hydrothermal process to fabricate superhydrophobic hydroxyapatite coatings and determination of their properties, Surf. Coat. Technol. 334 (2018) 84–89, https://doi.org/10.1016/j.surfcoat.2017.11.007.
[39] S.M.R. Razavi, J. Oh, S. Sett, L. Feng, X. Yan, M.J. Hoque, A. Liu, R.T. Haasch, M. Masoomi, R. Bagheri, N. Miljkovic, Superhydrophobic surfaces made from naturally derived hydrophobic materials, ACS sustain, Chem. Eng. 5 (2017) 11362–11370, https://doi.org/10.1021/acssuschemeng.7b02424.
[40] J.S. Benjamin, Mechanical alloying — A perspective, Met. Powder Rep. 45 (1990) 122–127, https://doi.org/10.1016/S0026-0657(10)80124-9.
[41] S.L. James, C.J. Adams, C. Bolm, D. Braga, P. Collier, T. Friščić, F. Grepioni, K.D. M. Harris, G. Hyett, W. Jones, A. Krebs, J. Mack, L. Maini, A.G. Orpen, I.P. Parkin, W.C. Shearouse, J.W. Steed, D.C. Waddell, Mechanochemistry: opportunities for new and cleaner synthesis, Chem. Soc. Rev. 41 (2012) 413–447, https://doi.org/10.1039/C1CS15171A.
[42] E. Gaffet, G. Le Caër, Mechanical Processing for Nanomaterials, in: H.S. Nalwa (Ed.), Encycl. Nanosci. Nanotechnol., American Scientific Publishers, 2004, pp. 1–39.
[43] E. MA, Alloys created between immiscible elements, Prog. Mater. Sci. 50 (2005) 413–509, https://doi.org/10.1016/j.pmatsci.2004.07.001.
[44] B. Bhushan, P.K. Katiyar, B.S. Murty, K. Mondal, Synthesis of hydrophobic Ni-VN alloy powder by ball milling, Adv. Powder Technol. 30 (2019) 1600–1610, https://doi.org/10.1016/j.apt.2019.05.007.
[45] P.A. Loginov, E.A. Levashov, V.V. Kurbatkina, A.A. Zaitsev, D.A. Sidorenko, Evolution of the microstructure of Cu–Fe–Co–Ni powder mixtures upon mechanical alloying, Powder Technol. 276 (2015) 166–174, https://doi.org/10.1016/j.powtec.2015.02.020.
[46] B. Bhoi, V. Srinivas, V. Singh, Evolution of microstructure and magnetic properties of nanocrystalline Fe70−xCuxCo30 alloy prepared by mechanical alloying, J. Alloy. Compd. 496 (2010) 423–428, https://doi.org/10.1016/j.jallcom.2010.01.155.
[47] C. Artieda-Guzmán, N. Llorca-Isern, Magnetic behaviour of nanocrystalline Cu–Fe–Co/Al2O3 composite powders obtained by mechanical alloying, J. Alloy. Compd. 580 (2013) 276–283, https://doi.org/10.1016/j.jallcom.2013.05.069.
[48] L. Jiesheng, Y. Yuanyuan, H. Xiang, Research on the preparation and properties of lauric acid/expanded perlite phase change materials, Energy Build. 110 (2016) 108–111, https://doi.org/10.1016/j.enbuild.2015.10.043.
[49] P.N. Nelson, R.A. Taylor, Powder X-ray diffraction, infrared and 13C NMR spectroscopic studies of the homologous series of some solid-state zinc(II) and sodium(I) n-alkanoates, Spectrochim. Acta Part A Mol. Biomol. Spectrosc. 138 (2015) 800–806, https://doi.org/10.1016/j.saa.2014.11.010.
[50] T. Zhang, J. Wu, Y. Xu, X. Wang, J. Ni, Y. Li, J.W. (Hans) Niemantsverdriet, Cobalt and cobalt carbide on alumina/NiAl(110) as model catalysts, Catal. Sci. Technol. 7 (2017) 5893–5899, https://doi.org/10.1039/C7CY01806A.
[51] S. Men, X. Jiang, X. Xiang, G. Sun, Y. Yan, Z. Lyu, Y. Jin, Synthesis of cellulose long-chain esters in 1-butyl-3-methylimidazolium acetate: structure-property relations, Polym. Sci. Ser. B. 60 (2018) 349–353, https://doi.org/10.1134/S1560090418030144.
[52] M.C. Biesinger, L.W.M. Lau, A.R. Gerson, R.S.C. Smart, Resolving surface chemical states in XPS analysis of first row transition metals, oxides and hydroxides: Sc, Ti, V, Cu and Zn, Appl. Surf. Sci. 257 (2010) 887–898, https://doi.org/10.1016/j.apsusc.2010.07.086.
[53] M.C. Biesinger, B.P. Payne, A.P. Grosvenor, L.W.M. Lau, A.R. Gerson, R.S.C. Smart, Resolving surface chemical states in XPS analysis of first row transition metals, oxides and hydroxides: Cr, Mn, Fe, Co and Ni, Appl. Surf. Sci. 257 (2011) 2717–2730, https://doi.org/10.1016/j.apsusc.2010.10.051.
[54] L. Hou, S. Bi, H. Zhao, Y. Xu, Y. Mu, Y. Lu, Electroless plating Cu-Co-P polyalloy on UV/ozonolysis irradiated polyethylene terephthalate film and its corrosion resistance, Appl. Surf. Sci. 403 (2017) 248–259, https://doi.org/10.1016/j.apsusc.2017.01.182.
[55] A.B.D. Cassie, S. Baxter, Wettability of porous surfaces, Trans. Faraday Soc. 40 (1944) 546, https://doi.org/10.1039/tf9444000546.
[56] K. Liu, L. Jiang, Bio-inspired self-cleaning surfaces, Annu. Rev. Mater. Res. 42 (2012) 231–263, https://doi.org/10.1146/annurev-matsci-070511-155046.
[57] W. Hao, J. Xu, R. Li, X. Zhao, L. Qiu, W. Yang, Developing superhydrophobic rock wool for high-viscosity oil/water separation, Chem. Eng. J. 368 (2019) 837–846, https://doi.org/10.1016/j.cej.2019.02.161.
[58] S. Woo, H.R. Park, J. Park, J. Yi, W. Hwang, Robust and continuous oil/water separation with superhydrophobic glass microfiber membrane by vertical polymerization under harsh conditions, Sci. Rep. 10 (2020) 21413, https://doi.org/10.1038/s41598-020-78271-9.
[59] S. Liu, Q. Xu, S.S. Latthe, A.B. Gurav, R. Xing, Superhydrophobic/superoleophilic magnetic polyurethane sponge for oil/water separation, RSC Adv. 5 (2015) 68293–68298, https://doi.org/10.1039/C5RA12301A.